

RESEARCH

Open Access



Senescent cell reduction does not improve recovery in mice under experimental autoimmune encephalomyelitis (EAE) induced demyelination

Zeeba Manavi¹, George S. Melchor^{1,2}, Meghan R. Bullard¹, Phillip S. Gross^{1,2}, Shinjini Ray¹, Pankaj Gaur³, Maryna Baydyuk¹ and Jeffrey K. Huang^{1,2*}

Abstract

Multiple sclerosis (MS) is a chronic inflammatory disease of the central nervous system (CNS) characterized by immune cell-driven demyelination and progressive neurodegeneration. Senescent cells (SCs) have recently been observed in chronic MS lesions indicating their possible involvement in disease progression. However, the role of SCs and the potential therapeutic benefit of their reduction through senolytic therapy remains to be determined in experimental autoimmune encephalomyelitis (EAE), a widely used preclinical model of MS. Here, we show that senescent-like myeloid cells accumulate in the spinal cord parenchyma and meninges in mice after myelin oligodendrocyte glycoprotein (MOG_{33–55}) EAE induction. Treatment with the senolytic cocktail, Dasatinib and Quercetin (DQ), effectively reduces the senescent-like myeloid cells, but this does not translate into improved clinical outcomes in EAE mice. Increasing DQ dosage or using INK-ATTAC transgenic mice also failed to ameliorate EAE severity. Additionally, histopathological analysis shows no significant differences in demyelination or axonal degeneration between treated and control groups. Our findings indicate that senescent-like myeloid cells are present in an immune-mediated demyelinating model of MS and can be reduced through senolytic therapy with Dasatinib and Quercetin. However, their reduction through DQ does not significantly impact inflammation or recovery, suggesting that the therapeutic potential of senolytics as disease-modifying drugs in MS may be limited.

Keywords Immune-mediated demyelination, Experimental autoimmune encephalomyelitis, Cellular senescence, Myeloid cells, Senolytics, Multiple sclerosis

Introduction

Multiple sclerosis (MS) is an immune-mediated chronic inflammatory disease of the central nervous system (CNS), characterized by the loss of myelin and axonal degeneration [1]. The clinical course of MS most often first presents as relapse-remitting MS (RRMS), which is characterized by periods of neurological disability (relapse) caused by adaptive immune system activation and demyelination, followed by recovery (remission) facilitated by the resolution of inflammation and remyelination [2, 3]. Individuals with MS eventually transition to

*Correspondence:

Jeffrey K. Huang

jeffrey.huang@georgetown.edu

¹ Department of Biology, Georgetown University, Washington, DC, USA

² Interdisciplinary Program in Neuroscience, Georgetown University, Washington, DC, USA

³ Department of Oncology, Georgetown University, Washington, DC, USA



© The Author(s) 2025. **Open Access** This article is licensed under a Creative Commons Attribution-NonCommercial-NoDerivatives 4.0 International License, which permits any non-commercial use, sharing, distribution and reproduction in any medium or format, as long as you give appropriate credit to the original author(s) and the source, provide a link to the Creative Commons licence, and indicate if you modified the licensed material. You do not have permission under this licence to share adapted material derived from this article or parts of it. The images or other third party material in this article are included in the article's Creative Commons licence, unless indicated otherwise in a credit line to the material. If material is not included in the article's Creative Commons licence and your intended use is not permitted by statutory regulation or exceeds the permitted use, you will need to obtain permission directly from the copyright holder. To view a copy of this licence, visit <http://creativecommons.org/licenses/by-nc-nd/4.0/>.

progressive MS (PMS), where they exhibit limited recovery periods and chronic neuroinflammation, driven by activated innate immune cells and the inability of myelin to regenerate, leading to extensive neurodegeneration and accumulating disability [3, 4].

Several studies have demonstrated the presence of senescent cells (SCs) in chronic MS lesions [5, 6]. Cellular senescence is a stress-induced irreversible cell-cycle arrest response triggered by advanced age [7] or chronic inflammation and observed in many neurodegenerative diseases [8–14]. While transient levels of senescence can be beneficial in repair [15, 16], their continued accumulation with aging or disease has been shown to have deleterious effects, as they can perpetuate inflammation and affect neighboring cells via paracrine SASP secretion [17, 18]. Since many hallmarks of PMS, such as DNA damage, oxidative stress, and danger-associated molecular patterns (DAMPs) [3, 19–21], are known drivers of cellular senescence, a feature of aging, it has been suggested that senescent cell (SC) accumulation in MS lesions results in prolonged inflammation through increased senescence-associated secretory phenotype (SASP) [22, 23]. These findings support the possibility that senescence may play a role in PMS and disease progression through prolonged inflammation and impaired remyelination. Therefore, decreasing SC burden may be a promising strategy for improving repair in MS. However, to date, the contribution of SCs and the efficacy of senolytic therapy to reduce SCs in immune-mediated inflammatory demyelination has not been fully explored.

Here, we examined the role of cellular senescence and its reduction in mice after MOG_{35–55} mediated experimental autoimmune encephalomyelitis (EAE) induction, a widely used preclinical model of MS. We observed the presence of senescent myeloid cells in demyelinated lesions at the chronic stage of the disease, particularly in the vicinity of the inflamed leptomeningeal space. Re-analysis of a previously published single-cell RNA sequencing dataset collected from MOG_{35–55} EAE CNS and meninges [24] revealed an increase in senescence-associated gene signatures [25] in myeloid lineage cells with disease progression. However, genetic depletion of SCs using the INK-ATTAC transgenic line [26], or their pharmacological depletion using Dasatinib and Quercetin (DQ), a known senolytic cocktail [27], was insufficient to improve functional outcomes in mice with EAE, despite significant reductions in senescent myeloid cells. Furthermore, histopathology analysis of DQ and vehicle treated animals did not reveal a significant difference in the extent of demyelination or axonal degeneration. Our findings suggest SCs represent a proportion of myeloid cells in EAE and do not appear to significantly contribute to inflammatory demyelination. Further studies are

needed to determine whether senolytic therapy, specifically DQ, could be effective in the treatment of MS.

Results

Canonical senescent markers increase in CNS meninges following EAE induction

Various CNS insults can trigger senescence, which has been suggested to contribute to disease pathogenesis [9, 10, 13]. Furthermore, stressors characteristic in MS, such as inflammation and oxidative stress, are also known inducers of senescence [19, 21, 23]. To determine whether cellular senescence occurs under immune-mediated demyelination, we induced experimental autoimmune encephalomyelitis (EAE) in 10–12-week-old female mice by immunizing them with myelin oligodendrocyte glycoprotein 35–55 (MOG_{35–55}) in complete Freund's adjuvant (CFA) and followed this with a pertussis toxin (PTX) injection (Fig. 1A). Next, we collected spinal cords from mice with EAE clinical score of 3 at 28 days post immunization (dpi), corresponding to the chronic phase of the disease, and from EAE naïve mice for analysis of common markers of senescence (Fig. 1A, see Additional file 2: Fig. S1 for score breakdown). We observed positive staining for several canonical senescent markers, including senescence-associated β -galactosidase (SA β -gal) (Fig. 1B), p16 and p21 (Fig. 1C) in EAE ventral white matter compared to naïve. While some p21 and p16 positive cells were observed in the gray matter and inside lesions, most were localized to the dural venous sinus and leptomeninges adjacent to ventral demyelinating lesions, as indicated by PDGFR β labeling of mural cells in the meningeal stromal niche [28] (Fig. 1D, E). The localization of senescent cells (SCs) to the meninges was confirmed using a p16^{tdTom} reporter line (Additional file 2: Fig. S2). Further, immunostaining analysis for p21 revealed its expression in the spinal cord throughout EAE disease development, with the highest expression observed at the chronic stage of the disease (28 dpi) (Additional file 2: Fig. S3). We did not observe co-labeling of p16 or p21 positive cells with Ki67, a marker for cell proliferation (Fig. 1F) or cleaved caspase-3 (CC3), a marker for apoptosis (Fig. 1G), suggesting these cells exhibited irreversible cell cycle arrest and resistance to apoptosis – both features of senescence [27]. Several studies suggest that glial cells such as oligodendrocyte lineage cells, the myelin producing cells in the CNS, and astrocytes may undergo age-induced or inflammation-induced senescence in MS, impairing their regenerative capacity following injury [23, 29–34]. However, we did not detect senescence markers in Olig2+ oligodendrocyte lineage cells (Additional file 2: Fig. S4). Similarly, these markers were also absent in Sox9⁺ astrocytes (Additional file 2: Fig. S4). Since the meningeal compartment harbors heterogeneous

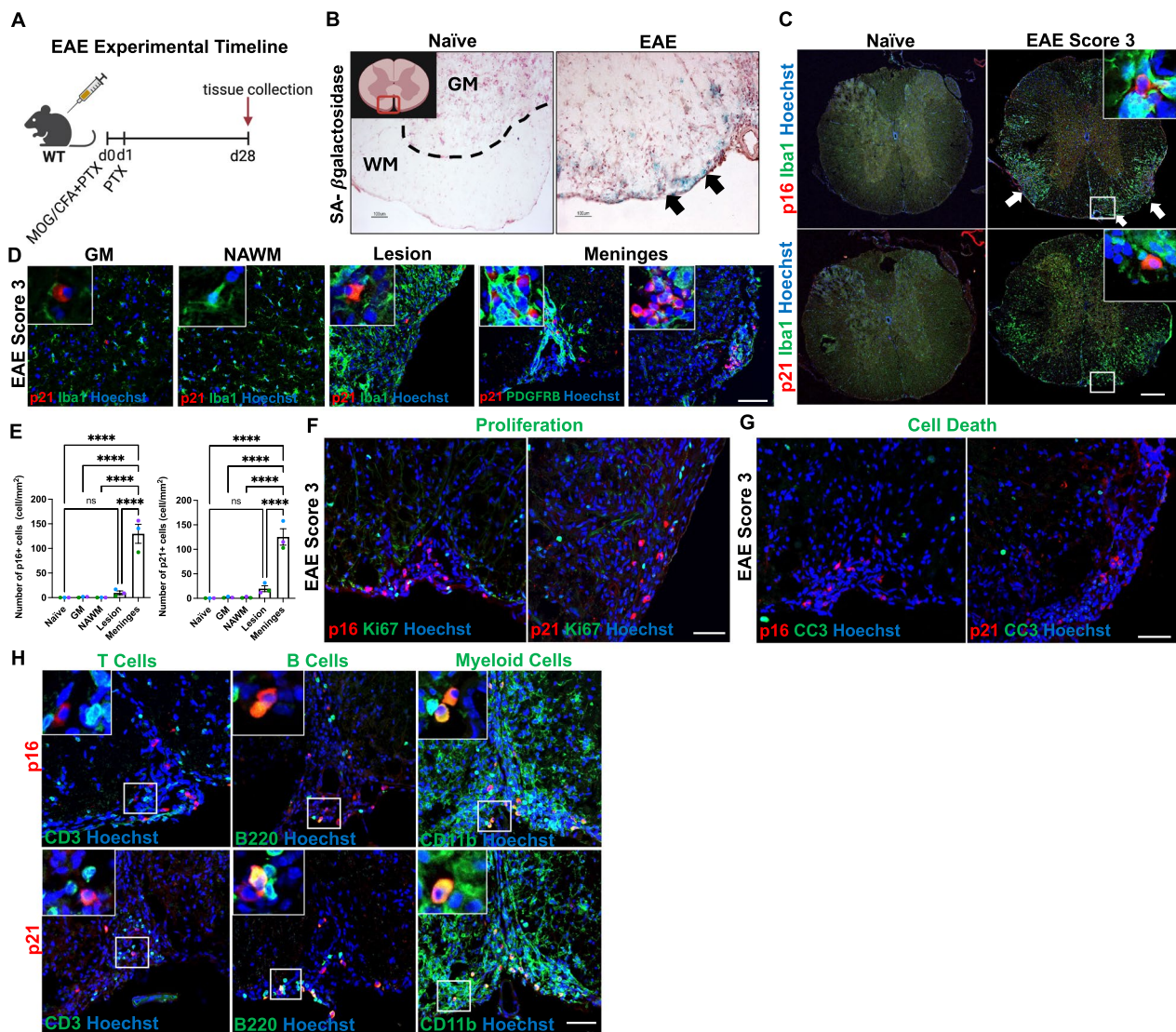


Fig. 1 Canonical senescent markers increase in CNS meningeal immune cells following EAE induction. **A** Schematic of EAE experimental timeline. Spinal cord tissue from mice with a score of 3 was collected at 28 days post-immunization (dpi). **B** Senescence-associated β-gal staining of naïve and EAE lumbar spinal cord shown with black arrows. **C** Naïve and EAE spinal cords stained with p16 and p21 are shown with white arrows, Iba1, and Hoechst nuclear stain. **D** Immunofluorescence (IF) staining of EAE spinal cord grey matter (GM), normal appearing white matter (NAWM), lesion, and leptomeninges with p21, Iba1 marker for microglia or PDGFRβ marker for mural cells, and Hoechst. **E** Quantification of d (one-way ANOVA with Tukey's multiple comparison test; $F_{(4,10)} = 45.51$, $df = 4$, $p < 0.0001$). **F** IF staining of EAE spinal cord for Ki67 marker for proliferation, and **G** cleaves caspase 3 (CC3) marker for apoptosis. **H** IF staining of lumbar EAE spinal cord with p21 and p16 with markers for T cells (CD3), B cells (B220), myeloid cells (CD11b). Data are presented as \pm SEM; $n = 3$ biological replicates, ns = not significant, **** $P < 0.0001$. Scale bars: b, 100 μm; c, 200 μm; d, f, g, h 20 μm

immune cell types involved in CNS immune surveillance [35–38], and meningeal inflammation is a key feature of progressive multiple sclerosis (PMS) [39, 40] and a PMS animal model [41], we next examined immune cell subpopulations. We observed the expression of p16 and p21 in B220⁺ B cells and CD11b⁺ myeloid cells, but not in CD3⁺ T cells (Fig. 1H). These results indicate cellular senescence occurs in select immune cell subpopulations

within the leptomeningeal compartment following EAE induction.

Myeloid cells are the primary immune cells expressing the p21 senescence marker

To identify which immune cells may be undergoing senescence, we analyzed p21 expression in fluorescence-activated single cell (FACS) sorted immune cells from

the spinal cord and meninges of mice with EAE at 28 dpi, corresponding to the chronic stage of the disease, and compared them to naïve mice. We gated on live CD45 immune cells, and identified two distinct p21-expressing populations – one with dim/intermediate fluorescent intensity (p21^{interm}) and another with bright/high fluorescent intensity (p21^{hi}) (Fig. 2A). We observed no

significant difference in the relative percentage of both p21^{hi}CD45⁺ subpopulations in the EAE spinal cord compared to naïve tissue (Fig. 2B). However, the total number of both p21^{hi}CD45⁺ subpopulations was significantly higher in mice with EAE than in naïve mice (Fig. 2C). This observation was also consistent when the two populations were combined (Additional file 2: Fig. S5). To

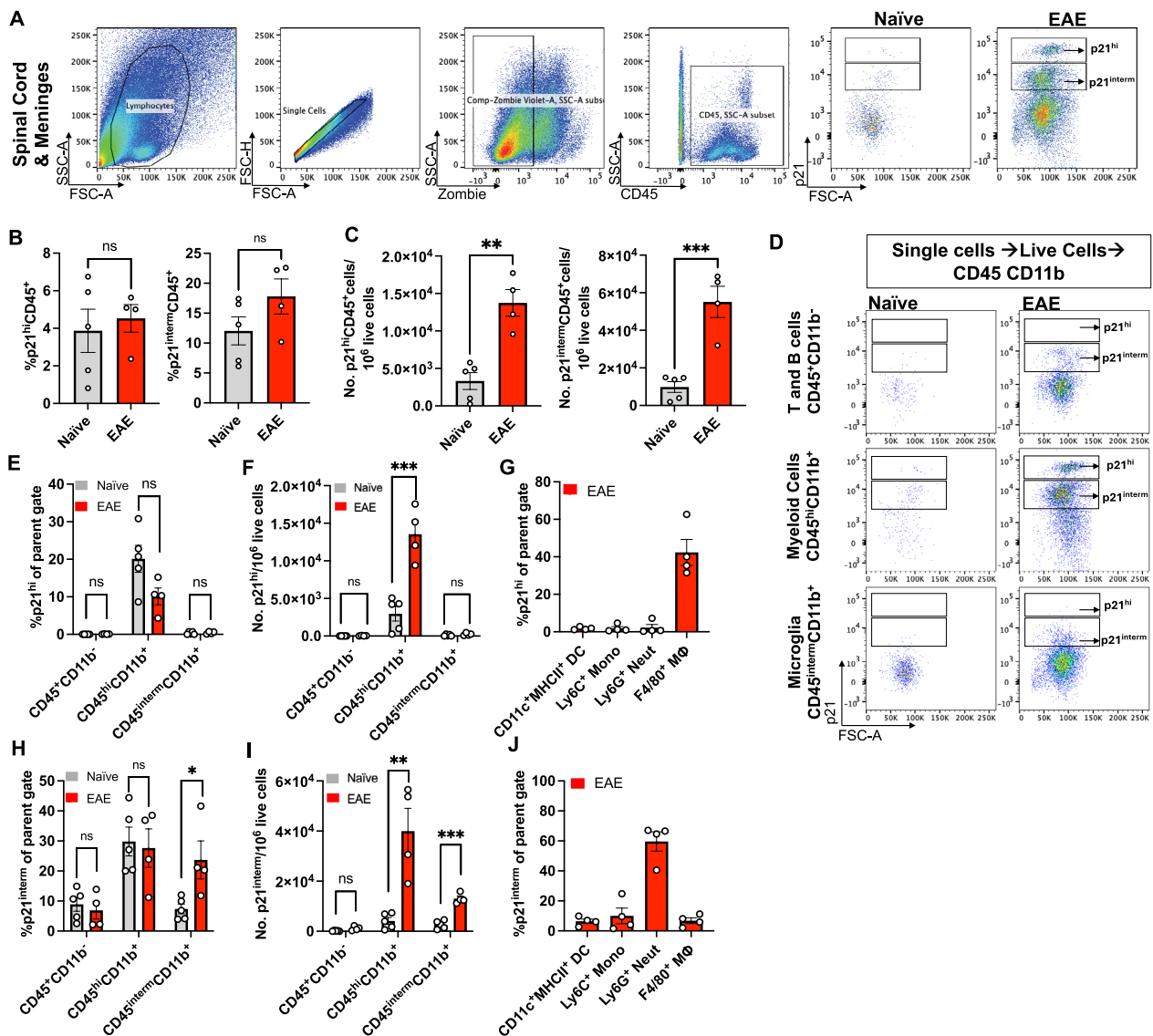


Fig. 2 Myeloid cells are the primary immune cells expressing the p21 senescence marker. **A** Flow cytometry analysis of p21 population in naïve and EAE spinal cord and meninges at 28 dpi under CD45⁺ gate. **B** Percentage of p21^{hi} (two-tailed t test; $t = 0.4539$, $df = 7$, $p = 0.6637$) and p21^{interm} (two-tailed t test; $t = 1.560$, $df = 7$, $p = 0.1626$). **C** Numbers of p21^{hi} (two-tailed t test; $t = 5.159$, $df = 7$, $p = 0.0013$) and p21^{interm} (two-tailed t test; $t = 5.669$, $df = 7$, $p = 0.0008$). **D** Flow cytometry analysis of p21^{hi} and p21^{interm} populations gated on T and B cells (CD45⁺CD11b⁻), myeloid cells (CD45^{hi}CD11b⁺), and microglia (CD45^{interm}CD11b⁺). **E** Quantification of percentage of p21^{hi} shown in d. **F** Numbers of p21^{hi} shown in d (two-tailed t test; $t = 5.523$, $df = 7$, $p = 0.0009$). **G** Percent p21^{hi} population under different myeloid cell populations. DC: dendritic cells, Mono: monocytes, Neut: neutrophils, MΦ: macrophages. **H** Quantification of percentage of p21^{interm} shown in d (two-tailed t test; $t = 2.795$, $df = 7$, $p = 0.0267$). **I** Numbers of p21^{interm} shown in d (two-tailed t test; $t = 4.414$, $df = 7$, $p = 0.0031$). **J** Percent p21^{interm} under different myeloid cell populations. Data are presented as \pm SEM, $n = 4$ –5 biological replicates, ns = not significant, * $P < 0.05$, ** $P < 0.01$, *** $P < 0.001$, **** $P < 0.0001$

determine which cell populations corresponded to p21^{hi} and p21^{interm}, we assessed p21 expression in total T and B cells (CD45⁺CD11b⁻), myeloid cells (CD45^{hi}CD11b⁺), and microglia (CD45^{interm}CD11b⁺) (Fig. 2D). In the spinal cord of EAE compared to naïve mice, we did not observe a significant difference in the percentage of p21^{hi} among the different immune populations (Fig. 2E). Conversely, we observed a significant increase in the number of infiltrating myeloid cells, with no differences observed in microglia or T and B cells (Fig. 2F), suggesting that p21^{hi} myeloid cells increase with EAE. Myeloid cells are a heterogeneous population that have been reported to acquire a senescent phenotype under chronic inflammatory conditions [42–46]. Among CD45^{hi}CD11b⁺ myeloid cell subsets (see Additional file 2: Fig. S6 for gating strategy), we found that 42.35% of F4/80⁺ macrophages exhibited p21^{hi} expression, with little to no expression observed in CD11c⁺/MHCII⁺ dendritic cells, Ly6C⁺ monocytes, or Ly6G⁺ neutrophils (Fig. 2G). We also quantified the distribution of p21^{interm} in immune cells and found that the percentage of p21^{interm} significantly increases in microglia, but not in other myeloid cells or T and B cells (Fig. 2H). Furthermore, the total number of p21^{interm} microglia and myeloid cells increased significantly in mice with EAE compared to naïve mice (Fig. 2I). Among the CD45^{hi}CD11b⁺ myeloid cell subsets, we found that 59.65% of Ly6G⁺ neutrophils expressed p21^{interm} with much lower expression observed in dendritic cells, monocytes and macrophages (Fig. 2J). Although the absolute number of myeloid cells was greater than that of lymphocytes in EAE (Additional file 2: Fig. S7), the percentage of myeloid cells expressing p21 was higher than in lymphocytes in EAE. Together, these results suggest EAE induction leads to an increase in the number of p21 expressing macrophages (p21^{hi}CD45^{hi}CD11b⁺), neutrophils (p21^{interm}CD45^{hi}CD11b⁺), and microglia (p21^{interm}CD45^{interm}CD11b⁺).

Myeloid cell recruitment into the CNS is closely associated with the severity of EAE [47, 48]. Given that neutrophils are blood-derived and tissue-resident macrophages can originate from circulating monocytes, we next sought to investigate whether p21-expressing myeloid cells are also present in peripheral immune organs, particularly the spleen, of mice induced with MOG_{35–55} EAE. The spleen plays a critical role in immune surveillance and serves as a reservoir for immune cells that can migrate to inflamed tissues [48, 49]. To assess the presence of senescent myeloid cells in the periphery, we performed flow cytometry on spleen samples from both naïve and EAE mice at 28 dpi. As observed in the spinal cord, we identified two distinct p21-expressing populations (p21^{hi} and p21^{interm}) in the EAE spleen, both of which showed a significant increase in percentage and

number compared to naïve tissue (Additional file 2: Fig. S8A–C). p21^{hi} was predominantly observed in peripheral Ly6C⁺ monocytes (Additional file 2: Fig. S8D–G), while p21^{interm} was observed in both Ly6C⁺ monocytes and Ly6G⁺ neutrophils (Additional file 2: Fig. S8D, H–J). These findings indicate the p21-expressing splenic neutrophils and monocytes observed in mice with EAE may be a contributing source to the CNS p21-expressing neutrophils and macrophages, possibly due to myelopoiesis in the bone marrow followed by recruitment to the CNS [48]. Overall, these data highlight the complex dynamics of immune senescence in EAE, particularly within the myeloid cell compartment.

Myeloid cells display an increase in the SenMayo gene signature with disease progression

Since there is no universal marker for senescence, a combination of senescence-associated markers is commonly used to identify SCs in vivo [50, 51]. These markers include, but are not limited to, markers for cell-cycle arrest like cyclin-dependent kinase (CDK) inhibitor proteins, including p16^{Ink4a} and p21^{CIP1}, senescence-associated β -galactosidase (SA β -gal) activity, and senescence-associated secretory phenotype (SASP) factors, including chemokines, cytokines, growth factors, or tissue remodeling proteases. Recently, the SenMayo gene signature has emerged as a valuable tool for identifying SCs [25]. This curated set of 125 genes in humans and 119 in mice was developed from multiple studies to capture SCs, particularly those with a SASP profile, across different tissues and species. To confirm the presence of senescent-like cells in EAE, we applied the SenMayo geneset to an existing single cell RNA sequencing (scRNAseq) data set collected from MOG_{35–55} EAE tissue [24] as an unbiased representation of senescent immune cell populations in the context of immune-mediated demyelination.

After quality control and filtering, scRNAseq yielded a total of 788 transcriptomic profiles in EAE spinal cord leptomeninges. Unsupervised clustering in naïve control tissue and across EAE tissues with increasing severity revealed 6 distinct cell types that were labelled according to known marker genes (Fig. 3A, B). As expected, we observed an increase in myeloid cell populations at the onset and peak of EAE not seen in naïve and preclinical mice (Fig. 3A). Using the SenMayo geneset (Additional File 1; Table 1), we showed that the majority of SCs are myeloid cells (Fig. 3C), and that senescence were highest at onset and peak EAE scores (Fig. 3D). SC gene expression, particularly by monocyte-derived macrophages and microglia, increased with EAE disease severity (Fig. 3E). We next compared *Cdkn1a* expression across myeloid cell types and EAE status, a widely used marker for SCs

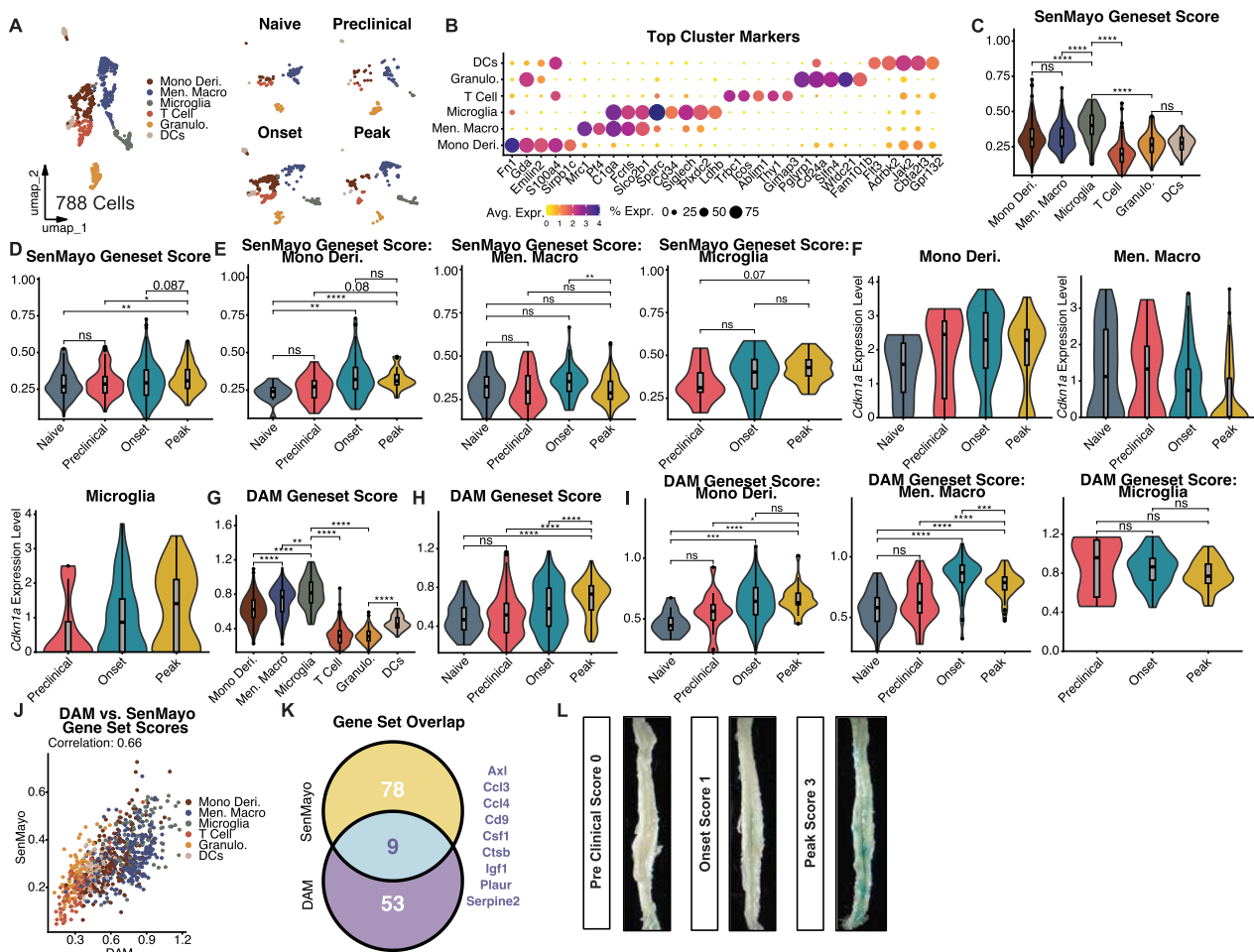


Fig. 3 Myeloid cells display an increase in the SenMayo gene signature with disease progression. **A** UMAP plot of 788 annotated leptomeningeal cells (left), split by EAE status (right). **B** Dot plot showcasing top marker genes of annotated CD45⁺ cell populations. **C** Violin plots depicting the SenMayo gene set score in the leptomeninges grouped by annotated CD45⁺ subclusters. **D** Violin plots depicting the SenMayo gene set score in the leptomeninges grouped by naïve, preclinical, onset, and peak EAE status. **E** Violin plots depicting the SenMayo gene set score in Monocyte Derived Macrophages (left), Meningeal Macrophages (center), and Microglia (right) grouped by naïve, preclinical, onset, and peak sample EAE status. **F** Violin plots with boxplot depicting *Cdkn1a* expression in 3 myeloid cell subtypes in the leptomeninges grouped by naïve, preclinical, onset, and peak EAE status. **G** Violin plots depicting the DAM gene set score in the leptomeninges grouped by annotated CD45⁺ subclusters. **H** Violin plots depicting the DAM gene set score in the leptomeninges grouped by naïve, preclinical, onset, and peak EAE status. **I** Violin plots depicting the DAM gene set score in Monocyte Derived Macrophages (left), Meningeal Macrophages (center), and Microglia (right) grouped by naïve, preclinical, onset, and peak EAE status. **J** Feature scatter plot showing the positive correlation between increasing DAM geneset scores and SenMayo geneset scores across all annotated cell types. **K** Venn diagram showing the 9 overlapping genes between the DAM and SenMayo genesets used to derive geneset scores, indicating that the two genesets are largely unique. **L** Senescence-associated β -gal staining of intact EAE spinal cord at pre-clinical, onset, and peak of the disease. Image taken at 63X magnification. For violin plots of *Cdkn1a* expression, a box plot is plotted for each violin plot corresponding to EAE status. For all violin plots of geneset scores (C-E, G-I), a box plot is plotted, and the medians have been compared to assess statistical significance, using the Wilcoxon non-parametric test followed by Bonferroni correction. ns = not significant, * $P < 0.05$, ** $P < 0.01$, *** $P < 0.001$, **** $P < 0.0001$

[52, 53]. We found that similar to the SenMayo gene signature, SC expression increased across myeloid cell types with EAE progression, particularly in monocyte derived macrophages and microglia (Fig. 3F). We also compared SenMayo geneset expression with a disease-associated microglia (DAM) related geneset (Additional File 1; Table 2) [54, 55]. Unsurprisingly, myeloid cell populations

expressed the highest DAM gene signature (Fig. 3G), and at higher expression levels than SenMayo throughout EAE progression (Fig. 3C, D, G, H). Activated monocyte-derived macrophage and meningeal macrophage DAM gene expression increased with disease severity (Fig. 3I). We further observed a positive correlation between SenMayo and DAM geneset scores (Fig. 3J), however only

9 genes overlapped between the genesets (Fig. 3K), suggesting that myeloid activation and senescence may be two independent characteristics of the myeloid populations in EAE. Furthermore, our SA β -gal staining of intact EAE spinal cord at the different stages of the disease parallels the overall myeloid findings from the Sen-Mayo and DAM gene signatures suggesting a correlation between SA β -gal senescence marker and disease severity (Fig. 3L). Taken together, these data suggest that myeloid cells with a senescent gene signature increase with disease progression.

Senolytics deplete senescent-like myeloid cells but are not sufficient to improve EAE outcome

Pharmacological or genetic clearance of SCs has been shown to attenuate neurodegeneration and CNS inflammation. Notably, the depletion of SCs has been shown to reduce brain inflammation and rejuvenate the immune cell landscape in aged mice [56]. However, whether clearance of SCs is beneficial in reducing inflammation and clinical disability in EAE remains to be investigated. In line with previous studies, we next asked whether senolytic treatment with Dasatinib and Quercetin (DQ) treatment reduces senescent-like myeloid cell burden and improves motor function in EAE. To this end, we treated naïve and EAE mice with DQ (5 mg/kg Dasatinib and 50 mg/kg Quercetin) or vehicle daily by oral gavage at the onset of the disease for 10 consecutive days (Fig. 4A). This dosage was shown to effectively eliminate SCs in vivo according to previously published data [27, 56, 57]. Mouse clinical scores and weights were monitored daily from the start of the treatment at the onset of clinical disability (9–14 dpi) until 11 days post treatment (dpt), followed by tissue collection at 11 dpt for flow cytometry and histology analysis. We observed no significant change in the disease severity or weights between DQ treated and control groups (Fig. 4B, C). Furthermore, increasing the dosage to 40 mg/kg of Dasatinib and 50 mg/kg of Quercetin, which has previously been reported to reduce MOG_{35–55}-EAE [58] and PLP_{139–151}-EAE [59] disease severity when administered separately also had no effect on clinical score (*data not shown*). Similarly, we found prophylactic treatment with DQ (Additional file 2: Fig. S9A–C) or the pharmacological depletion of SCs using the synthetic drug AP20187 (AP) in the INK-ATTAC mouse line [26] after EAE induction did not alter disease outcome (Additional file 2: Fig. S9D, E).

To determine if DQ treatment depleted senescent-like myeloid cells, flow cytometry analysis for the level of CD4 and CD8 T cells (CD45⁺CD11b⁻; CD4CD8), myeloid cells (CD45^{hi}CD11b⁺), and microglia (CD45^{interm}CD11b⁺) was performed on spleen and

spinal cord at 11 dpt (Fig. 4D). We observed a significant decrease in the spinal cord in the percentage and number of p21^{hi} macrophages (Fig. 4E, F) but not in p21^{interm} neutrophils (Fig. 4E, G). Similarly, in the spleen, we observed a significant decrease in the percentage of p21^{hi} Ly6C⁺ monocytes, with no change detected in p21^{interm} neutrophils (Additional file 2: Fig. S10A–C). However, unlike in the spinal cord, there is a trend toward an increase in the overall myeloid cell population between the two groups, but this increase was not statistically significant (Additional file 2: Fig. S10D). Furthermore, in the spinal cord, the relative proportion of p21^{interm} microglia decreased, while the absolute number of p21^{interm} microglia remained unchanged (Fig. 4H, I). Additionally, the proliferation rate and cell death within EAE spinal cord lesions was not significantly different between the treatment groups as shown by Ki67 (Additional file 2: Fig. S11A, B) and CC3 stains (Additional file 2: Fig. S11C, D). These findings suggest that DQ may be reducing p21 expression in microglia rather than inducing cell death. To further interrogate this possibility, we measured the mean fluorescent intensity (MFI) of p21 in the microglia population and observed a significant reduction in DQ compared to vehicle-treated EAE mice (Fig. 4J). To assess whether SC reduction led to improved histopathology, we examined axonal integrity in EAE spinal cords by staining for NF200 (phosphorylated neurofilament) and SMI32 (non-phosphorylated neurofilament). Analysis of the relative signal intensity of SMI-32 normalized to NF200 revealed no significant differences in axonal dystrophy between the treatment groups (Additional file 2: Fig. S12A, B). Additionally, Luxol fast blue (LFB), utilized to evaluate demyelination, also did not show statistically significant difference in demyelination between the two groups (Additional file 2: Fig. S12C, D). We further did not observe a significant change in the proportion of CD4 and CD8 lymphocytes following DQ treatment (Fig. 4K), suggesting that DQ is only affecting the myeloid cell compartment.

Together, our findings indicate that DQ treatment does not exhibit disease-modifying properties in EAE (Fig. 4B). Interestingly DQ appears to have a selective effect on senescent-like myeloid cells. Specifically, DQ depletes p21^{hi} macrophages (Fig. 4F), with no impact on the p21^{interm} neutrophil population (Fig. 4G), and it appears to be reducing the proportion of p21 expressing microglia without any apparent induced cell death (Fig. 4I).

Discussion

Cellular senescence is a well-established mechanism that prevents tumorigenesis by inducing irreversible cell cycle arrest triggered by telomere shortening.

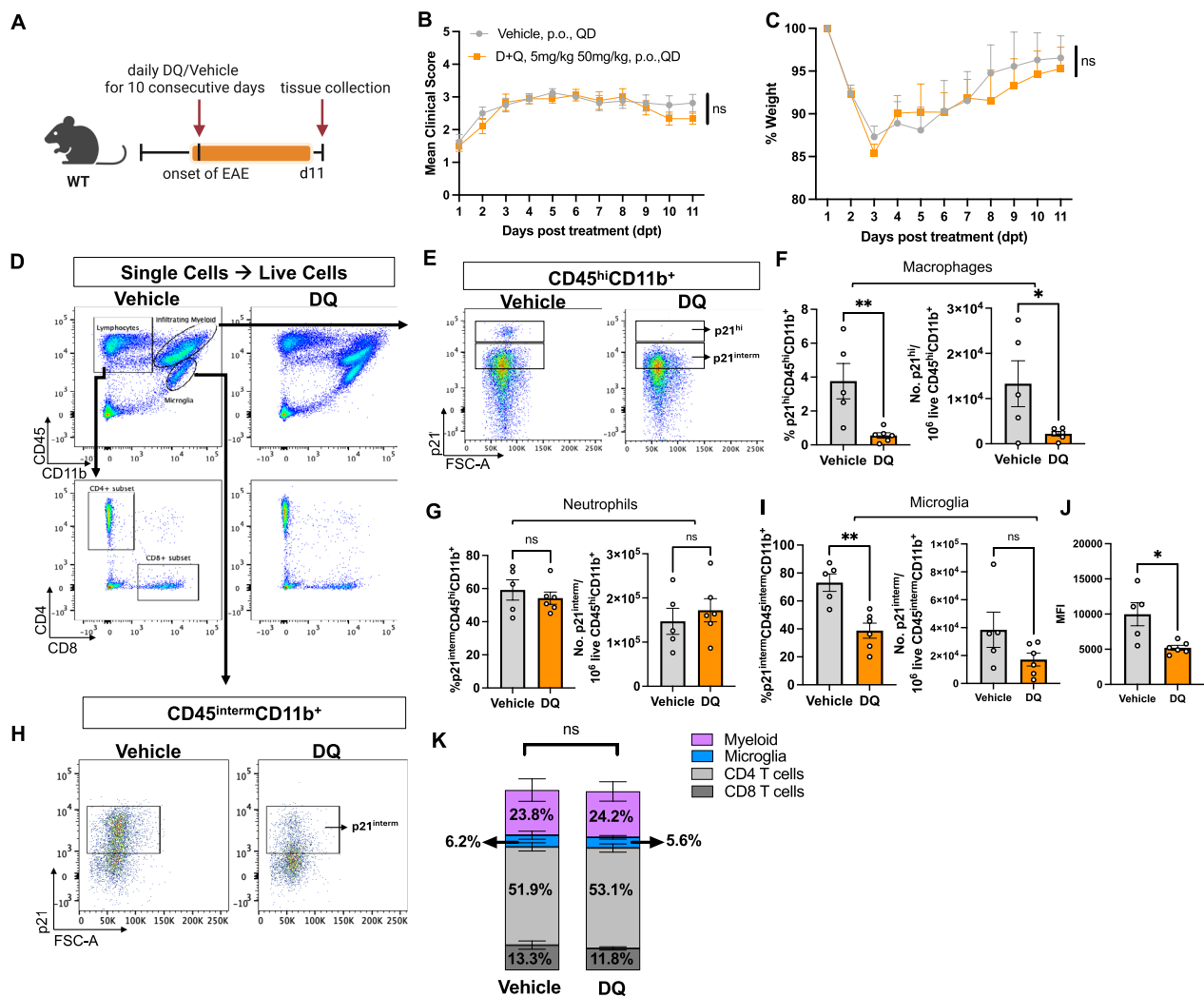


Fig. 4 Senolytics deplete senescent-like myeloid cells but are not sufficient to improve EAE outcome. **A** Schematic of EAE experimental timeline treated with vehicle or DQ (5 mg/kg, 50 mg/kg) for 10 consecutive days. Spinal cord and meninges were collected at 11 days post treatment (dpt) for flow cytometry analysis. **B** EAE mean clinical score of vehicle (n=8) and DQ (n=9) treated mice over time (Man-Whitney U test; p=0.4807, two-tailed). **C** The percentage of baseline averaged weight over time (Man-Whitney U test; p=0.67331, two-tailed). **D** Gating strategy for evaluation of CD4 and CD8 T cells (CD45⁺CD11b⁻; CD4CD8), myeloid cells (CD45^{hi}CD11b⁺), and microglia (CD45^{interm}CD11b⁺). **E** Flow cytometry analysis of p21^{hi} and p21^{interm} myeloid under CD45^{hi}CD11b⁺ parent gate. **F** Quantification of p21^{hi} macrophages shown (two-tailed t test; for percentage t=3.345, df=9, p=0.0086; for counts t=2.396, df=9, p=0.0401) and **G** p21^{interm} neutrophils (two-tailed t test; t=0.7175, df=9, p=0.4913; t=0.6311, df=9, p=0.5437) shown in e. **H** Flow cytometry analysis of p21^{interm} microglia under CD45^{interm}CD11b⁺ gate. **I** Quantification of p21^{interm} microglia shown in g (two-tailed t test; t=4.186, df=9, p=0.0024; t=1.219, df=9, p=0.2538). **J** MFI of p21 in microglia. **K** Overall proportion of immune cells (two tailed t test; myeloid p=0.9614, microglia p=0.6222, CD4 cells p=0.7179, and CD8 cells p=0.4520) post treatment. Data are presented as ± SEM, n=5–6 biological replicates, ns=not significant, *P<0.5, **P<0.01

However, when immune-mediated clearance of senescent cells (SCs) fails to take place, SCs accumulate, leading to aging [7] and age-related conditions such as cardiovascular disease [60], osteoarthritis [61], diabetes [62], and disc degeneration [57] among others. The prominence of SCs in various conditions led to the development of senolytic therapy that selectively target and deplete SCs with minimal effects on quiescent and

proliferative cells, which have been shown to extend lifespan and ameliorate age-related conditions.

Senescence can also be induced independent of age, often as result of injury or under chronic inflammatory conditions as seen in Parkinson’s disease [10], stroke [12], traumatic brain injury [11], and AD [13, 14, 63], which may have both age-dependent and age-independent related SC accumulation. Importantly, these studies show

SC depletion mitigates neurodegenerative processes, underscoring the therapeutic potential of senolytic therapy for treatment of neurodegenerative diseases. Dasatinib and Quercetin (DQ), a known senolytic cocktail, is currently being tested for efficacy in Alzheimer's disease [64, 65]. While these findings represent a step toward novel therapeutic strategies, further studies are necessary to establish the efficacy and safety of senolytic therapy before clinical trial testing in a broader range of neurodegenerative conditions. In the context of MS, contribution of SCs and the potential benefit of senolytic therapy remains to be elucidated. While a few important studies suggest a role for senescence in MS [5, 6, 23, 33], and its animal models [21, 43, 66, 67], the specific role of SCs in immune-mediated demyelination and the effect of senolytic therapy such as DQ has not been fully described.

In the current study, we found SCs accumulated in MOG_{35–55} induced EAE and identified three primary myeloid cell subsets in the CNS displaying senescent-like features: CD45^{hi}CD11b⁺ F4/80⁺ macrophages with high p21 expression, and CD45^{hi}CD11b⁺ Ly6G⁺ neutrophils and CD45^{interm}CD11b⁺ microglia with intermediate p21 expression. Previous studies have also observed the presence of p21 high and intermediate populations [68–71]. Whether senescent markers expressed in these cells indicate a true senescent state or a different physiological response to injury and inflammation remains unclear. It has been reported that p21 expression in neutrophils and macrophages may be induced independent of senescence. For example, in neutrophils, p21 is required for neutrophil NET formation [72], while in macrophages, it is suggested to be required for the transition from the M1 to M2 phenotype [73, 74]. In fact, there are ongoing discussions as to whether macrophages exhibiting senescence markers should be classified as senescent [60, 75, 76] or senescent-like/activated [73, 77]. This distinction is challenging because of the overlap between senescence genes and stress-associated genes upregulated in activated immune cells during inflammation [78]. In line with this, Cellular Senescent network (SenNet) and other groups have recognized this concern, noting that activated monocytes and macrophages, are producers of SASP factors such as IL-1 α , IL-1 β , IL-6, and HMGB1, which can lead to their misclassification as a senescent population by the SenMayo gene panel [51]. Indeed, in our EAE single cell RNA sequencing re-analysis, we observed monocyte-derived macrophages, meningeal macrophages, and microglia enriched for the SenMayo panel and disease associated microglial (DAM) genes, highlighting the need for careful characterization of these cells as to whether they are senescent or simply upregulating stress-associated genes in response to injury, which coincidentally overlap with SASP factors. While it has been challenging

to classify activated macrophages as SCs, there is growing evidence demonstrating that in Alzheimer's disease (AD) models a subpopulation of disease-associated microglia (DAMs), and not monocyte-derived (CCR2⁺) or border associated-macrophages (Mrc1⁺), may enter a senescent state upon injury and inflammation [44, 45], in which DAMs that undergo proliferative exhaustion become senescent [71]. Overall, our data demonstrates that MOG_{35–55} EAE captures p21-expressing myeloid cell populations which may be senescent or senescent-like/activated. Several studies have shown that both microglia and macrophages may represent a senescent population implicated in the aging brain [68, 69, 79] and in MS and its animal models [5, 6, 21, 43, 66, 67]. Notably, a recent study showed that the senolytic drug ABT-263 is able to improve recovery in mice with EAE [66]. However, we found here that DQ treatment or the pharmacological reduction of SCs in INK-ATTAC mice was insufficient to alleviate disease severity or neuropathology associated with MOG_{35–55} EAE. It remains unclear why ABT-263 is more effective in improving recovery from EAE compared to DQ. One possibility is that the therapeutic effectiveness of senolytics depends on the specific cell types or pathways targeted by senolytic drugs, as not all senolytics are equally effective at inducing senolysis [80, 81].

Recent work from our lab [43] indicates that DQ was more effective in enhancing remyelination in young mice compared to aged mice, suggesting other inflammatory factors may be inhibiting remyelination. Therefore, while senolysis may reduce senescent cells in EAE, the ongoing inflammatory environment observed in this model, much like in aged tissues, may limit its therapeutic efficacy. In both cases, it is not simply the presence of senescent cells that inhibits recovery, but also the broader inflammatory context and the presence of additional inhibitory factors that may prevent the efficiency of repair mechanisms. Additionally, it is known that middle-aged mice with EAE experience more severe disease progression and widespread microglial activation compared to younger mice [82]. However, it remains unclear whether aging leads to an increase in senescence markers within the microglial population and whether DQ treatment could be more beneficial in older animals. It is possible that the inflammatory environment in aged EAE tissue, similar to the age of lyssolecithin demyelination [43], may already impose a significant barrier to remyelination, limiting the potential benefits of senolysis in such contexts.

The inability of DQ to enhance clinical recovery in mice with EAE might also be attributed to the fundamental differences observed between MS and its preclinical model. It is important to note that the MOG_{35–55} EAE model does not fully replicate the pathological features of progressive MS [83–85]. MOG_{35–55} EAE in C57BL/6 and

nonobese diabetic (NOD) mice primarily model an acute, monophasic disease with chronic stabilization of deficits, rather than the slow, progressive degeneration seen in progressive MS [86, 87]. As a result, this model imposes limitations on our understanding of the potential role of cellular senescence and the therapeutic effects of senolytic therapy in progressive MS. Thus, the development of animal models that more closely resemble progressive MS is crucial to determining whether reducing chronic SC accumulation can enhance CNS repair or recovery in progressive MS, where disease progression occurs behind a closed blood–brain barrier with compartmentalized inflammation [88]. Furthermore, in recent years, there has been growing discussion that the pathology of MOG_{35–55} EAE resembles that of myelin-oligodendrocyte-associated demyelinating disease (MOGAD) [89]. Therefore, one could argue that the strategy using Dasatinib and Quercetin in MOG_{35–55}-mediated EAE may be a more appropriate model for MOGAD rather than MS. Future investigations may benefit from exploring senolytics in combination with disease-modifying therapy or using models that more accurately reflect PMS to better understand the role of senescent macrophages and microglia in disease progression.

Materials and methods

Mice

All experiments were performed according to the protocol approved by the Institutional Animal Care and Use Committee (IACUC) at Georgetown University. Mice were housed in a pathogen-free barrier environment throughout the study. Cages were maintained on a 12-h light/dark cycle with food and water ad libitum. C57BL/6 mice (RRID: IMSR_JAX:000664) were purchased from The Jackson Laboratory. p16^{tdTom} mice were purchased from the NIH Mutant Mouse Resource & Research Center and bred as heterozygotes with C57BL/6 mice. Heterozygote p16^{tdTom} mice were used for all experiments. p16 INK-ATTAC mice were purchased from Unity Biotechnology and bred and used as homozygotes. All experiments were performed on female mice 9–12 weeks old.

Experimental autoimmune encephalomyelitis (EAE)

C57BL/6 female mice (Jackson Laboratory) at age 9–12 weeks were acclimatized for 7 days prior to EAE. EAE was induced according to the Hooke Laboratories protocol (EK-2110). Briefly, mice were immunized by two 100ul subcutaneous injections of an emulsion of MOG_{35–55} in complete Freund's adjuvant (CFA) (Day 0), followed by administration of 200 ng pertussis toxin (PTX) in 1X phosphate-buffered saline (PBS) intraperitoneally on the day of immunization (Day 0), and again, the

following day (Day 1). The mice were scored daily from EAE Day 7 until the end of the experiment. Mice were scored according to the Hook Lab protocol as follows: 0.0=no obvious changes in motor function; 0.5=tip of tail is limp; 1.0=limp tail; 1.5=limp tail and hind leg inhibition; 2.0=limp tail and weakness of hind legs or signs of head tilting; 2.5=limp tail and dragging of hind legs or strong head tilting; 3.0=limp tail and complete paralysis of hind legs or limp tail with paralysis of one front and one hind leg; 3.5=limp tail and complete paralysis of hind legs plus mouse unable to right itself when placed on its side; 4.0=limp tail, complete hind leg and partial front leg paralysis, mouse is minimally moving but appears alert and feeding; 4.5=complete hind and partial front leg paralysis, no movement around the cage, mouse is not alert; 5.0=mouse is found dead due to paralysis or mouse is euthanized due to severe paralysis.

Senolytic treatments

For Dasatinib and Quercetin (DQ) treatment studies, wildtype;EAE mice were randomly assigned to Dasatinib (5 mg/kg, ThermoFischer, 462320010) and Quercetin (50 mg/ml, ThermoFischer, 174070100) or vehicle (5% DMSO, 30% PEG400, 5% tween 80, and 60% water). DQ or vehicle at the equal volume of 100 ul was administered via oral gavage at the onset of the disease (score 1) for 10 consecutive days. The clinical scores and weight of mice were recorded daily from the start of the treatment.

For AP20187 (AP) treatment, INK-ATTAC;EAE mice were administered AP (2 mg/kg, MedchemExpress B/B homo-dimerizer, HY-13992) or vehicle (4% DMSO, 10% PEG400, 1.72% tween 20). AP, or vehicle, was injected intraperitoneally twice a week from the day of immunization (day 0). The clinical scores and weight of mice were recorded daily from the start of the treatment.

Senescence associated β -galactosidase staining (SA β -gal)

SA β -gal was performed according to the manufacturer's protocol (Cell Signaling, 98605) with modifications. Mice were first perfused with ice-cold 1X PBS, and the spinal cord tissue was then embedded in O.C.T., followed by flash freeze, and then immediately sectioned and processed for SA β -gal per the manufacturer's instructions. The tissue sections were stained with Nuclear Fast Red counterstain stain (Bioenno, 003034), followed by a PBS wash, and mounted with Fluoromount-G (Southern Biotech 0100-01). For the SA β -gal staining of the intact tissue, mice were perfused with 4% PFA, post-fixed in PFA for 30 min, and washed with PBS before transferring to β -gal staining solution (pH=5.9). Images were taken on OLYMPUS cellSens at 63 \times magnification.

Flow cytometry (FCM)

Spinal cords with meninges and spleens were collected from EAE mice in RPMI 1640 (Gibco, 11835030) and mechanically dissociated. Briefly, the spleen was homogenized by passing through a 70 µm cell strainer and rinsed with 1X PBS. The samples were then incubated in RBC Lysis Buffer for 10 min, and were then deactivated, and washed with PBS. Cells were resuspended in PBS for 10^6 cells/100 µl reaction. The spinal cord was finely chopped and digested in Accutase (Sigma-Aldrich, A6964) for 30 min at 37°. Homogenized tissue was passed through a 100 µm cell strainer and rinsed with RPMI 1640 supplemented with 10% FBS (Sigma-Aldrich, 12306C). Myelin debris were removed next using a 40% Percoll gradient (Sigma-Aldrich, P1644) at 650 g for 25 min at room temperature. Cells were washed with PBS and generated 10^5 – 10^6 live cells per 100 µl reaction. Cells from spleens and spinal cords were then incubated with Live/Dead Zombie Violet staining, followed by cell surface staining. FcR block was added to the cells and incubated for 10 min before adding the following cell surface antibodies with monocyte blocker: CD45 BV650, CD11b APC Cy7, CD11c BV785, MHC II BV510, Ly6C BV605, Ly6G PerCP Cy5, F4/80 FITC, CD3 PE Cy7, B220 BV711. For intracellular staining, cells were incubated in Fixation Buffer and then permeabilized using Intracellular Permeabilization Buffer before incubating with p21 antibody (Santacruz, sc-6246, AF680). Cells were gated at the Georgetown Lombardi Comprehensive Cancer Center Flow Cytometry and Cell Sorting Shared Resource (FCSR). All reagents and antibodies were purchased from BioLegend unless noted otherwise. Cells were analyzed on the BD LSRFortessa flow cytometer at the Georgetown Lombardi Comprehensive Cancer Center Flow Cytometry and Cell Sorting Shared Resource. The flow cytometry results were analyzed using FlowJo™ v10.10.0 Software (BD Life Sciences).

Immunofluorescent (IF)

Mice were perfusion-fixed with 4% (w/v) paraformaldehyde (Sigma-Aldrich) in PBS. Spinal cord tissue was dissected and postfixed in 4% PFA for 30 min. Tissue was cryoprotected in 30% (w/v) sucrose (Sigma) in PBS before freezing in Tissue-Tek O.C.T. compound (Sakura) on dry ice. Frozen tissues were cut into 12 µm sections with cryostat and collected on SuperFrost®Plus slides (VWR International) and were allowed to dry for 1 h before storing at –80 °C. For immunostaining, the sectioned tissues were dried for 1 h at room temperature (RT), and ImmEdge Hydrophobic Barrier PAP pen was used to draw boundaries around the tissue. Sections were washed with TBST (0.05% Tween 20 in 1X TBS) and subsequently with TBS (1X TBS in PBS), and then

permeabilized for 5 min with permeabilization solution (1% Triton X-100 in 1X TBS). Sections were then incubated in blocking solution (10% Donkey serum 0.25% (v/v) Triton™ X-100 in 1X TBS) for 1 h at RT, followed by MOM IgG blocking solution (Vector laboratories) for 1 h at RT before adding the following primary antibodies: rabbit anti-Iba1 (Fujifilm Wako, 019-19741, 1:400), mouse anti-p16 (Abcam, ab54210, 1:500), mouse anti-p21 (Santa Cruz, sc6246, 1:500), goat anti-PDGFRβ (R&D systems, AF1042, 1:200), rat anti-CD3 (eBioscience, 14-0032-85, 1:100), rat anti-B220 (Invitrogen, 14-0452-81, 1:100), rat anti-CD11b (Biorad MCA74G, 1:100), rabbit anti-Olig2 (Millipore Sigma, AB9610, 1:300), rabbit anti-Sox9 (EMD Millipore, AB5535, 1:1500), rabbit anti-RFP (Rockland Immunochemicals 600-401-379, 1:1000) or rabbit anti-DsRd (Clontech, 632496, 1:500), rabbit anti-KI67 (ThermoFischer Scientific, PA5-19462, 1:200), rabbit anti-cleaved-caspase-3 (Cell Signaling, 9661S, 1:100), mouse anti-NF200 (Sigma-Aldrich, N4142, 1:100), and rabbit anti-SMI32 (BioLegend, 801702, 1:500). Slides were then washed in TBST and TBS before being incubated for 1 h in the dark at RT with the following fluorescent conjugated secondary antibodies: Alexa Fluor 488 (Invitrogen, 1:1000), Alexa Fluor 594 (Invitrogen, 1:500) and Hoechst 33342 (Invitrogen, 1:20,000). Following incubation, the slides were washed again in TBST and TBS before being mounted with Fluoromount-G mounting medium. Primary and secondary antibodies were diluted in blocking solution and applied to sections. For the detection of Olig2, antigen retrieval was performed before immunostaining with 1X Antigen Unmasking Solution (Vector laboratories).

Luxol fast blue stain (LFB)

LFB stain and analysis was performed by Hook Laboratories. OCT embedded cryosectioned slides were prefixed in 10% neutral buffered formalin and rinsed in distilled water. Slides were placed in 0.1% LFB solution overnight at 60 °C. The slides rinsed with 95% alcohol followed by distilled water distilled water and briefly placed in 0.05% lithium carbonate solution. The slides were then differentiated in a 70% alcohol solution and rinsed with water followed by 0.1% cresyl violet stain for 1 min. The Spinal cord sections were scored by Hook Lab pathologist as follows: 0—no demyelination (less than 5% demyelinated area), 1—5–20% demyelinated area, 2—20–40% demyelinated area, 3—40–60% demyelinated area, 4—60–80% demyelinated area, 5—80–100% demyelinated area.

Re-analysis of mouse EAE scRNA-sequencing data

The published single cell dataset of isolated CD45+ cells from various CNS compartments in mouse EAE (GSE118948) was used to validate the appearance of

senescent-like cells during MOG_{35–55} EAE. Processed data files were acquired directly from Gene Expression Omnibus, and the subsequent quality control, dimensionality reduction, clustering, and analyses were performed using Seurat (v5.1.0) in R (v4.4.1). All data were converted to SeuratObjects using the CreateSeuratObject() function, retaining genes expressed in at least 5 cells. Metadata to assess quality control and group data were applied to SeuratObjects, and filtering was conducted to exclude cells with low UMI counts (nUMI < 1500), probable doublets (nUMI > 20,000), low quality determined by large percentage expression of *Kcnq1ot1* (percent *Kcnq1ot1* >= 2.0), and low quality determined by large percentage expression of mitochondrial genes (percent_mito > 10.0). After quality control, all samples were merged, totaling 3,748 cells and 13,681 genes for downstream analysis. The merged data were normalized using the SCTransform() function [90, 91] in Seurat (variable features = 2,000, vst.flavor = “v2”). At this point, quality control was assessed on a cluster basis and a second round of filtration occurred to exclude clusters low in gene numbers with near absent expression of *Ptprc* (CD45), indicative of CD45 negative cellular contamination. The remaining 2,883 nuclei were re-normalized, as described above, clustered (dimensions = 1:20, resolution = 0.3), and annotated according to the original article. The leptomeningeal compartment (788 nuclei) was subset, clustered, and annotated, as described above (exception: resolution = 0.2). Annotated final clustering was projected onto a UMAP using the dimplot() function. Marker genes were calculated using the FindAllMarkers() function, and chosen based on ranked adjusted p-value. Gene signature scores are based on the SenMayo senescence geneset [25] and DAM related genes [54, 55]. Scores were calculated by the aggregate normalized sum expression of the SenMayo genes (87 genes) and DAM genes (62 genes) found in the overall dataset per nuclei barcode (Additional file 1: Data Tables 1 & 2), and were plotted using scCustomize (v2.1.2, DOI: 10.5281/zenodo.5706430). P values in violin plots were calculated using compare_means() from the ggpubr package (v0.6.0), using the Wilcoxon non-parametric test followed by Bonferroni correction for multiple comparisons. P values were then plotted using stat_pvalue_manual() from the ggpubr package (v0.6.0). ns = not significant, *P ≤ 0.05, **P ≤ 0.01, ***P ≤ 0.001, ****P ≤ 0.0001.

Experimental design, imaging and statistical analyses

Images were taken on a Zeiss LSM 800 completed system confocal imager. Lumbar spinal cord collected from mice were used for immunostaining analysis. For SA β-gal imaging, a minimum of four images were analyzed from n = 1 mice per group. Images were taken on OLYMPUS

cellSens at 63X magnification. EAE lesions were located by visualizing the accumulation of Hoechst-positive nuclei within the dorsal and ventral white matter. Meninges were visualized using PDGFRβ vascular staining. A minimum of three lesions/section (3 sections/slide) from n = 3 mice were analyzed for p16 and p21 cell density. To calculate the area of NAWM, the GM area was subtracted from the lesion area. Area was calculated using Zeiss Zen software. Density per square millimeter was calculated in Microsoft Excel. All statistics were performed using GraphPad Prism. Data are expressed as mean ± SEM. Comparisons were analyzed by, one-way ANOVA with Tukey’s multiple comparison test, or two-tailed t test. EAE score and weight comparison were performed using the Man-Whitney U test.

Abbreviations

ABT-263	Navitoclax
AD	Alzheimer’s disease
AP	AP20187 B/B homodimerizer
CC3	Cleaved-caspase 3
CDK	Cyclin-dependent kinase
CNS	Central nervous system
DAM	Disease-associated microglia
DAMPs	Danger-associated molecular patterns
DQ	Dasatinib and quercetin
EAE	Experimental autoimmune encephalomyelitis
GM	Grey matter
LFB	Luxol fast blue
MFI	Mean fluorescent intensity
MOG	Myelin oligodendrocyte glycoprotein
MOGAD	Myelin oligodendrocyte glycoprotein antibody-associated disease
MS	Multiple sclerosis
NAWM	Normal appearing white matter
PMS	Progressive MS
RRMS	Relapse-remitting MS
SA β-gal	Senescence-associated β-galactosidase
SASP	Senescence-associated secretory phenotype
ScRNAseq	Single cell RNA sequencing
SCs	Senescent cells
SenMayo	Senescence-associate gene signature
TBI	Traumatic brain injury

Supplementary Information

The online version contains supplementary material available at <https://doi.org/10.1186/s12974-025-03425-3>.

Additional file 1. Table 1. SenMayo gene signature. Table 2. Disease-associated microglia gene set.

Additional file 2: Fig. S1. Clinical course of EAE mice utilized for the characterization of the senescent cells in the spinal cord. The clinical scores of individual animals and the average clinical score of animals used for immunostaining analysis in Fig. 1. The peak of disease severity, indicated by the highest clinical scores, was observed between 14 and 17 dpi. All mice reached a clinical score of 3 by the experimental endpoint (28 dpi). **Fig. S2.** Increase in p16^{tdTom} positive cells in CNS meninges following EAE induction. Spinal cord section of p16^{tdTom}+ naive and EAE induced with MOG_{35–55} EAE stained with DsRed and Hoechst. Scale bar: 200 μm. **Fig. S3.** Senescence hallmarks increase in EAE spinal cord with clinical score progression. IHC staining of lumbar EAE spinal cord with p21 (red) Iba (green) and Hoescht at onset, peak, and chronic stage. Quantification of p16 (one-way ANOVA with Tukey’s multiple comparison test; $F_{(2,6)} = 76.90$, $df = 6$, $p < 0.0001$) and p21

(one-way ANOVA with Tukey's multiple comparison test; $F_{(2,6)} = 52.73$, $df = 6$, $p = 0.0001$) in EAE and naïve spinal cord. Data are presented as \pm SEM, ns = not significant, $***P < 0.01$, $****P < 0.0001$. Scale bars: 200 μ m and 10 μ m. **Fig. S4.** Senescent markers are not expressed by oligodendrocyte lineage cells and astrocytes. Immunofluorescence staining of lumbar EAE spinal cord with p21 and p16, Olig2 markers for oligodendrocyte lineage cells and Sox9 marker for astrocytes. Scale bar: 20 μ m. **Fig. S5.** Combined analysis of p21 subpopulations in the spinal cord of EAE and naïve mice. Percentage (two-tailed t test; $t = 1.517$, $df = 7$, $p = 0.1731$) and total number (two-tailed t test; $t = 6.429$, $df = 7$, $p = 0.0004$) of combined p21 populations assessed by flow cytometry. Data are presented as \pm SEM, $n = 4$ –5 biological replicates, ns = not significant, $****P < 0.0001$. **Fig. S6.** Gating strategy and immunophenotyping of spinal cord. Gating strategy for evaluation of live single cell populations. Gating is as follows: $CD45^+CD11b^-$ gate for T and B cells, $CD45^{hi}CD11b^+$ for myeloid cells, $CD45^{interm}CD11b^+$ for microglia, $CD45^{hi}CD11b^+CD11c^+MHCII^+$ for dendritic cells $CD45^{hi}CD11b^+Ly6C^+Ly6G^-$ for monocytes, $CD45^{hi}CD11b^+Ly6C^-Ly6G^+$ for neutrophils, and $CD45^{hi}CD11b^+Ly6C^-Ly6G^+F4/80^+$ macrophages. p21 was analyzed under the described gates. **Fig. S7.** Comparison of absolute counts of myeloid cells versus lymphocytes in EAE. Absolute count of myeloid and lymphocyte cell populations assessed by flow cytometry (two-tailed t test; $t = 2.686$, $df = 6$, $p = 0.0363$). Data are presented as \pm SEM, $n = 4$ biological replicates, ns = not significant, $*P < 0.05$. **Fig. S8.** Increase in p21 positive peripheral myeloid cells in EAE spleen. **(A)** Flow cytometry analysis of p21 population in naïve and EAE spleen at 28 dpi under $CD45^+$ gate. **(B)** Percentage of $p21^{hi}$ (two-tailed t test; $t = 3.612$, $df = 7$, $p = 0.0086$) and $p21^{interm}$ (two-tailed t test; $t = 11.58$, $df = 7$, $p < 0.0001$). **(C)** Numbers of $p21^{hi}$ (two-tailed t test; $t = 3.500$, $df = 7$, $p = 0.010$) and $p21^{interm}$ (two-tailed t test; $t = 11.81$, $df = 7$, $p < 0.0001$). **(D)** Flow cytometry analysis of $p21^{hi}$ and $p21^{interm}$ gated on T and B cells ($CD45^+CD11b^-$), and peripheral myeloid cells ($CD45^{hi}CD11b^+$). **(E)** Quantification of percentage of $p21^{hi}$ shown in d (two-tailed t test; $t = 4.070$, $df = 7$, $p = 0.0047$). **(F)** Numbers of $p21^{hi}$ shown in d (two-tailed t test; $t = 5.813$, $df = 7$, $p = 0.0007$). **(G)** Percent $p21^{hi}$ population under monocytes (Mono) and neutrophils (Neut). **(H)** Quantification of percentage of $p21^{interm}$ shown in d. **(I)** Numbers of $p21^{hi}$ shown in d (two-tailed t test; $t = 12.12$, $df = 7$, $p < 0.0001$). **(J)** Percent of $p21^{interm}$ population under monocytes and neutrophils. Data are presented as \pm SEM, $n = 4$ –5 biological replicates, ns = not significant, $*P < 0.05$, $**P < 0.01$, $****P < 0.0001$. **Fig. S9.** Prophylactic depletion of the senescent population using genetic and pharmacological approaches does not improve EAE clinical score. **(A)** The experimental timeline of WT;EAE mice treated with vehicle or DQ (5 mg/kg, 50 mg/kg) daily by oral gavage at the onset of the disease for 14 consecutive days. **(B)** EAE mean clinical score of vehicle- and DQ-treated mice over time (Man-Whitney U test; $p = 0.6061$, two-tailed). **(C)** The percentage of baseline weight over time averaged across vehicle ($n = 8$) and DQ ($n = 5$) treatment (Man-Whitney U test; $p = 0.6730$, two-tailed). **(D)** The experimental timeline of INK-ATTAC;EAE mice treated with vehicle or 2 mg/kg AP daily post immunization for 28 days. **(E)** EAE mean clinical score of INK-ATTAC;EAE mice treated with vehicle ($n = 4$) and AP ($n = 4$) over time (Man-Whitney U test; $p = 0.8857$, two-tailed). **Fig. S10.** Senolytic treatment with Dasatinib and Quercetin in EAE spleen. **(A)** Gating strategy for evaluation of splenic CD4 and CD8 T cells ($CD45^+CD11b^-$; $CD4CD8$) and peripheral myeloid cells ($CD45^{hi}CD11b^+$). **(B)** Flow cytometry analysis of $p21^{hi}$ population under $CD45^{hi}CD11b^+$ parent gate. **(C)** Quantification of $p21^{hi}$ and $p21^{interm}$ cells shown in b (two-tailed t test; $t = 2.285$, $df = 9$, $p = 0.0482$). **(D)** Overall proportion of immune cells. Data are presented as \pm SEM, $n = 5$ –6 biological replicates, ns = not significant, $*P < 0.05$. **Fig. S11.** DQ treatment does not affect the rate of proliferation or cell death in EAE spinal cord. **(A)** IF staining of EAE lumbar spinal cord for Ki67, CD11b, and Hoechst. **(B)** Quantification of a (two-tailed t test; $t = 0.4797$, $df = 5$, $p = 0.6517$). **(C)** Staining of EAE spinal cord for cleaves caspase 3 (CC3), CD11b, and Hoechst. **(D)** Quantification of c (two-tailed t test; $t = 1.209$, $df = 5$, $p = 0.2808$). Scale bar, 50 μ m. Data are presented as \pm SEM, $n = 3$ –4 biological replicates, ns = not significant. **Fig. S12.** Histopathological assessment of EAE spinal cord following Vehicle or DQ treatment. **(A)** IF staining of EAE lumbar spinal cord for NF200 phosphorylated neurofilament, SMI32 marker

for non-phosphorylated neurofilament, and Hoechst. SMI-32+NF200+ co-labelling indicates axonal dystrophy. **(B)** Relative SMI-32 signal intensity normalized to NF200 and average lesion size showing comparable lesions between the two groups. **(C)** Luxol fast blue staining of lumbar spinal cord sections demonstrates the extent of demyelination (light blue/pale) compared to intact myelin (dark blue). **(D)** Percent demyelination was calculated as the ratio of demyelinated area to total white matter area. Scale bar, 50 μ m. Data are presented as \pm SEM, unpaired t-test, ns = not significant.

Acknowledgements

We thank Lombardi Comprehensive Cancer Center Flow Cytometry and Cell Sorting Shared Resources at Georgetown for FACS data collection, Dr. Darren J. Baker of Mayo Clinic, and members of the Huang lab for comments on this project.

Author contributions

Z.M. and J.K.H. designed the study. Z.M. performed all mouse experiments and data analysis. G.S.M. and M.R.B. conducted the RNAseq re-analysis. P.S.G., S.R., and P.G. contributed to mouse experiments and analysis. M.B. contributed to experimental design. Z.M. drafted the manuscript. J.K.H. and G.S.M. edited the manuscript. J.K.H. oversaw the study.

Funding

This study was supported by NCATS/NIH Training Fellowship (TL1TR001431) to Z.M. and NINDS/NIH (5R01NS107523, 2R56NS107523-06), NIA/NIH (1R21AG072327) and National Multiple Sclerosis Society (NMSS) Harry Weaver Neuroscience Scholar Award (JF-1806–31381) to J.K.H.

Data availability

No datasets were generated or analysed during the current study.

Declarations

Ethics approval and consent to participate

Not applicable.

Consent for publication

Not applicable.

Competing interests

The authors declare no competing interests.

Received: 3 January 2025 Accepted: 21 March 2025

Published online: 07 April 2025

References

- Reich DS, Lucchinetti CF, Calabresi PA. Multiple sclerosis. *N Engl J Med*. 2018;378(2):169–80.
- Dutta R, Trapp BD. Relapsing and progressive forms of multiple sclerosis: insights from pathology. *Curr Opin Neurol*. 2014;27(3):271–8.
- Lassmann H, van Horssen J, Mahad D. Progressive multiple sclerosis: pathology and pathogenesis. *Nat Rev Neurol*. 2012;8(11):647–56.
- Franklin RJM, Ffrench-Constant C. Remyelination in the CNS: from biology to therapy. *Nat Rev Neurosci*. 2008;9(11):839–55.
- Absinta M, Maric D, Gharagozloo M, Garton T, Smith MD, Jin J, et al. A lymphocyte–microglia–astrocyte axis in chronic active multiple sclerosis. *Nature*. 2021;597(7878):709–14.
- Nicaise AM, Wagstaff LJ, Willis CM, Paisie C, Chandok H, Robson P, et al. Cellular senescence in progenitor cells contributes to diminished remyelination potential in progressive multiple sclerosis. *Proc Natl Acad Sci*. 2019;116(18):9030.
- Baker DJ, Childs BG, Durik M, Wijers ME, Sieben CJ, Zhong J, et al. Naturally occurring p16Ink4a-positive cells shorten healthy lifespan. *Nature*. 2016;530(7589):184–9.

8. Baker DJ, Petersen RC. Cellular senescence in brain aging and neurodegenerative diseases: evidence and perspectives. *J Clin Invest*. 2018;128(4):1208–16.
9. Bussian TJ, Aziz A, Meyer CF, Swenson BL, van Deursen JM, Baker DJ. Clearance of senescent glial cells prevents tau-dependent pathology and cognitive decline. *Nature*. 2018;562(7728):578–82.
10. Chinta SJ, Woods G, Demaria M, Rane A, Zou Y, McQuade A, et al. Cellular senescence is induced by the environmental neurotoxin paraquat and contributes to neuropathology linked to Parkinson's disease. *Cell Rep*. 2018;22(4):930–40.
11. Schwab N, Taskina D, Leung E, Innes BT, Bader GD, Hazrati LN. Neurons and glial cells acquire a senescent signature after repeated mild traumatic brain injury in a sex-dependent manner. *Front Neurosci*. 2022;16:1027116. <https://doi.org/10.3389/fnins.2022.1027116>.
12. Torres-Querol C, Torres P, Vidal N, Portero-Otín M, Arque G, Purroy F. Acute ischemic stroke triggers a cellular senescence-associated secretory phenotype. *Sci Rep*. 2021;11(1):15752.
13. Zhang P, Kishimoto Y, Grammatikakis I, Gottmukkala K, Cutler RG, Zhang S, et al. Senolytic therapy alleviates A β -associated oligodendrocyte progenitor cell senescence and cognitive deficits in an Alzheimer's disease model. *Nat Neurosci*. 2019;22(5):719–28.
14. Bhat R, Crowe EP, Bitto A, Moh M, Katsetos CD, Garcia FU, et al. Astrocyte senescence as a component of Alzheimer's disease. *PLoS ONE*. 2012;7(9):e45069.
15. Demaria M, Ohtani N, Youssef SA, Rodier F, Toussaint W, Mitchell JR, et al. An essential role for senescent cells in optimal wound healing through secretion of PDGF-AA. *Dev Cell*. 2014;31(6):722–33.
16. Storer M, Mas A, Robert-Moreno A, Pecoraro M, Ortells MC, Di Giacomo V, et al. Senescence is a developmental mechanism that contributes to embryonic growth and patterning. *Cell*. 2013;155(5):1119–30.
17. Coppé JP, Desprez PY, Krtolica A, Campisi J. The senescence-associated secretory phenotype: the dark side of tumor suppression. *Annu Rev Pathol Mech Dis*. 2010;5(1):99–118.
18. Kumari R, Jat P. Mechanisms of cellular senescence: cell cycle arrest and senescence associated secretory phenotype. *Front Cell Dev Biol*. 2021. <https://doi.org/10.3389/fcell.2021.645593>.
19. Choi IY, Lee P, Adany P, Hughes AJ, Belliston S, Denney DR, et al. In vivo evidence of oxidative stress in brains of patients with progressive multiple sclerosis. *Mult Scler J*. 2018;24(8):1029–38.
20. Fischer MT, Sharma R, Lim LJ, Haider L, Frischer JM, Drexhage J, et al. NADPH oxidase expression in active multiple sclerosis lesions in relation to oxidative tissue damage and mitochondrial injury. *Brain*. 2012;135(3):886–99.
21. Rouillard ME, Hu J, Sutter PA, Kim HW, Huang JK, Crocker SJ. The cellular senescence factor extracellular HMGB1 directly inhibits oligodendrocyte progenitor cell differentiation and impairs CNS remyelination. *Front Cell Neurosci*. 2022;16:833186. <https://doi.org/10.3389/fncel.2022.833186>.
22. Manouchehri N, Salinas VH, Rabi Yeganeh N, Pitt D, Hussain RZ, Stuve O. Efficacy of disease modifying therapies in progressive MS and how immune senescence may explain their failure. *Front Neurol*. 2022;13:854390.
23. Papadopoulos D, Magliozzi R, Mitsikostas DD, Gorgoulis VG, Nicholas RS. Aging, cellular senescence, and progressive multiple sclerosis. *Front Cell Neurosci*. 2020;14:178.
24. Jordão MJC, Sankowski R, Brendecke SM, Sagar LG, Tai YH, et al. Single-cell profiling identifies myeloid cell subsets with distinct fates during neuroinflammation. *Science*. 2019;363(6425):eaat7554.
25. Saul D, Kosinsky RL, Atkinson EJ, Doolittle ML, Zhang X, LeBrasseur NK, et al. A new gene set identifies senescent cells and predicts senescence-associated pathways across tissues. *Nat Commun*. 2022;13(1):4827.
26. Baker DJ, Wijshake T, Tchkonja T, LeBrasseur NK, Childs BG, van de Sluis B, et al. Clearance of p16 Ink4a-positive senescent cells delays ageing-associated disorders. *Nature*. 2011;479(7372):232–6.
27. Zhu Y, Tchkonja T, Pirtskhalava T, Gower AC, Ding H, Giorgadze N, et al. The Achilles' heel of senescent cells: from transcriptome to senolytic drugs. *Aging Cell*. 2015;14(4):644–58.
28. Rustenhoven J, Drieu A, Mamuladze T, de Lima KA, Dykstra T, Wall M, et al. Functional characterization of the dural sinuses as a neuroimmune interface. *Cell*. 2021;184(4):1000–1016.e27.
29. Neumann B, Baror R, Zhao C, Segel M, Dietmann S, Rawji KS, et al. Metformin restores CNS remyelination capacity by rejuvenating aged stem cells. *Cell Stem Cell*. 2019;25(4):473–485.e8.
30. Rivellini C, Porrello E, Dina G, Mrakic-Sposta S, Vezzoli A, Bacigaluppi M, et al. JAB1 deletion in oligodendrocytes causes senescence-induced inflammation and neurodegeneration in mice. *Ann Arbor: American Society for Clinical Investigation*; 2022.
31. Schlett JS, Mettang M, Skaf A, Schweizer P, Errerd A, Mulugeta EA, et al. NF- κ B is a critical mediator of post-mitotic senescence in oligodendrocytes and subsequent white matter loss. *Mol Neurodegener*. 2023;18(1):24.
32. Windener F, Grewing L, Thomas C, Dorion MF, Otteken M, Kular L, et al. Physiological aging and inflammation-induced cellular senescence may contribute to oligodendroglial dysfunction in MS. *Acta Neuropathol (Berl)*. 2024;147(1):82.
33. Kritsilis M, V. Rizou S, Koutsoudaki PN, Evangelou K, Gorgoulis VG, Papadopoulos D. Ageing, cellular senescence and neurodegenerative disease. *Int J Mol Sci*. 2018;19(10):2937.
34. Papadopoulos D, Magliozzi R, Bandiera S, Cimignolo I, Barusolo E, Probert L, et al. Accelerated cellular senescence in progressive multiple sclerosis: a histopathological study. *Ann Neurol*. 2025. <https://doi.org/10.1002/ana.27195>.
35. Cugurra A, Mamuladze T, Rustenhoven J, Dykstra T, Beroshvili G, Greenberg ZJ, et al. Skull and vertebral bone marrow are myeloid cell reservoirs for the meninges and CNS parenchyma. *Science*. 2021;373(6553):eabf7844.
36. Derk J, Jones HE, Como C, Pawlikowski B, Siegenthaler JA. Living on the edge of the CNS: meninges cell diversity in health and disease. *Front Cell Neurosci*. 2021;15:703944. <https://doi.org/10.3389/fncel.2021.703944>.
37. Mrdjen D, Pavlovic A, Hartmann FJ, Schreiner B, Utz SG, Leung BP, et al. High-dimensional single-cell mapping of central nervous system immune cells reveals distinct myeloid subsets in health, aging, and disease. *Immunity*. 2018;48(2):380–395.e6.
38. Van Hove H, Martens L, Scheyltjens I, De Vlaminck K, Pombo Antunes AR, De Prijck S, et al. A single-cell atlas of mouse brain macrophages reveals unique transcriptional identities shaped by ontogeny and tissue environment. *Nat Neurosci*. 2019;22(6):1021–35.
39. Absinta M, Vuolo L, Rao A, Nair G, Sati P, Cortese ICM, et al. Gadolinium-based MRI characterization of leptomeningeal inflammation in multiple sclerosis. *Neurology*. 2015;85(1):18–28.
40. Magliozzi R, Howell OW, Reeves C, Roncaroli F, Nicholas R, Serafini B, et al. A gradient of neuronal loss and meningeal inflammation in multiple sclerosis. *Ann Neurol*. 2010;68(4):477–93.
41. Pol S, Schweser F, Bertolino N, Preda M, Sveinsson M, Sudyn M, et al. Characterization of leptomeningeal inflammation in rodent experimental autoimmune encephalomyelitis (EAE) model of multiple sclerosis. *Exp Neurol*. 2019;314:82–90.
42. Fan Y, Zhang W, Huang X, Fan M, Shi C, Zhao L, et al. Senescent-like macrophages mediate angiogenesis for endplate sclerosis via IL-10 secretion in male mice. *Nat Commun*. 2024;15(1):2939.
43. Gross PS, Laforet VD, Manavi Z, Zia S, Lee SH, Shults N, et al. Senescent-like microglia limit remyelination through the senescence associated secretory phenotype. *BioRxiv Prepr Serv Biol*. 2024;2024.05.23.595605.
44. Ng PY, Zhang C, Li H, Baker DJ. Senescent microglia represent a subset of disease-associated microglia in P301S mice. *J Alzheimers Dis*. 2023;95(2):493–507.
45. Rachmian N, Medina S, Cherqui U, Akiva H, Deitch D, Edilbi D, et al. Identification of senescent, TREM2-expressing microglia in aging and Alzheimer's disease model mouse brain. *Nat Neurosci*. 2024;27(6):1116–24.
46. Wilk CM, Cathomas F, Török O, Le Berichel J, Park MD, Bigenwald C, et al. Circulating senescent myeloid cells infiltrate the brain and cause neurodegeneration in histiocytic disorders. *Immunity*. 2023;56(12):2790–2802.e6.
47. Melero-Jerez C, Alonso-Gómez A, Moñivas E, Lebrón-Galán R, Machín-Díaz I, de Castro F, et al. The proportion of myeloid-derived suppressor cells in the spleen is related to the severity of the clinical course and tissue damage extent in a murine model of multiple sclerosis. *Neurobiol Dis*. 2020;140:104869.
48. Shi K, Li H, Chang T, He W, Kong Y, Qi C, et al. Bone marrow hematopoiesis drives multiple sclerosis progression. *Cell*. 2022;185(13):2234–2247.e17.

49. Bronte V, Pittet MJ. The spleen in local and systemic regulation of immunity. *Immunity*. 2013;39(5):806–18.
50. Ogrodnik M, Carlos Acosta J, Adams PD, d'Adda Di Fagagna F, Baker DJ, Bishop CL, et al. Guidelines for minimal information on cellular senescence experimentation in vivo. *Cell*. 2024;187(16):4150–75.
51. Suryadevara V, Hudgins AD, Rajesh A, Pappalardo A, Karpova A, Dey AK, et al. SenNet recommendations for detecting senescent cells in different tissues. *Nat Rev Mol Cell Biol*. 2024;25:1–23.
52. López-Domínguez JA, Rodríguez-López S, Ahumada-Castro U, Desprez PY, Konovalenko M, Laberge RM, et al. Cdkn1a transcript variant 2 is a marker of aging and cellular senescence. *Aging*. 2021;13(10):13380–92.
53. Liu JY, Souroullas GP, Diekman BO, Krishnamurthy J, Hall BM, Sorrentino JA, et al. Cells exhibiting strong p16INK4a promoter activation in vivo display features of senescence. *Proc Natl Acad Sci U S A*. 2019;116(7):2603–11.
54. Hou J, Zhou Y, Cai Z, Terekhova M, Swain A, Andhey PS, et al. Transcriptomic atlas and interaction networks of brain cells in mouse CNS demyelination and remyelination. *Cell Rep*. 2023;42(4):112293.
55. Keren-Shaul H, Spinrad A, Weiner A, Matcovitch-Natan O, Dvir-Szternfeld R, Ulland TK, et al. A unique microglia type associated with restricting development of Alzheimer's disease. *Cell*. 2017;169(7):1276–1290.e17.
56. Zhang X, Pearsall VM, Carver CM, Atkinson EJ, Clarkson BDS, Grund EM, et al. Rejuvenation of the aged brain immune cell landscape in mice through p16-positive senescent cell clearance. *Nat Commun*. 2022;13(1):5671.
57. Novais EJ, Tran VA, Johnston SN, Darris KR, Roupas AJ, Sessions GA, et al. Long-term treatment with senolytic drugs Dasatinib and Quercetin ameliorates age-dependent intervertebral disc degeneration in mice. *Nat Commun*. 2021;12(11):5213.
58. Azizi G, Goudarzvand M, Afraei S, Sedaghat R, Mirshafey A. Therapeutic effects of dasatinib in mouse model of multiple sclerosis. *Immunopharmacol Immunotoxicol*. 2015;37(3):287–94. <https://doi.org/10.3109/08923973.2015.1028074>.
59. Muthian G, Bright JJ. Quercetin, a flavonoid phytoestrogen, ameliorates experimental allergic encephalomyelitis by blocking IL-12 signaling through JAK-STAT pathway in T lymphocyte. *J Clin Immunol*. 2004;24(5):542–52. <https://doi.org/10.1023/B:JOCI.0000040925.55682.a5>.
60. Childs BG, Baker DJ, Wijshake T, Conover CA, Campisi J, van Deursen JM. Senescent intimal foam cells are deleterious at all stages of atherosclerosis. *Science*. 2016;354(6311):472–7.
61. Faust HJ, Zhang H, Han J, Wolf MT, Jeon OH, Sadtler K, et al. IL-17 and immunologically induced senescence regulate response to injury in osteoarthritis. *J Clin Invest*. 2020;130(10):5493–507.
62. Helman A, Klochendler A, Azazmeh N, Gabai Y, Horwitz E, Anzi S, et al. p16(Ink4a)-induced senescence of pancreatic beta cells enhances insulin secretion. *Nat Med*. 2016;22(4):412–20.
63. Fancy NN, Smith AM, Caramello A, Tsartsalis S, Davey K, Muirhead RCJ, et al. Characterisation of premature cell senescence in Alzheimer's disease using single nuclear transcriptomics. *Acta Neuropathol (Berl)*. 2024;147(1):78.
64. Gonzales MM, Garbarino VR, Marques Zilli E, Petersen RC, Kirkland JL, Tchkonja T, et al. Senolytic therapy to modulate the progression of Alzheimer's disease (SToMP-AD): A Pilot Clinical Trial. *J Prev Alzheimers Dis*. 2022;9(1):22–9.
65. Riessland M, Ximerakis M, Jarjour AA, Zhang B, Orr ME. Therapeutic targeting of senescent cells in the CNS. *Nat Rev Drug Discov*. 2024;23:1–21.
66. Drake SS, Zaman A, Gianfelice C, Hua EML, Heale K, Afanasiev E, et al. Senolytic treatment diminishes microglia and decreases severity of experimental autoimmune encephalomyelitis. *J Neuroinflammation*. 2024;21(1):283.
67. Matsuda T, Nakano S, Konishi Y, Kawamoto S, Uemura K, Kondo T, et al. Cellular senescence in white matter microglia is induced during ageing in mice and exacerbates the neuroinflammatory phenotype. *Commun Biol*. 2023;6(1):1–13.
68. Ogrodnik M, Evans SA, Fielder E, Victorelli S, Kruger P, Salmonowicz H, et al. Whole-body senescent cell clearance alleviates age-related brain inflammation and cognitive impairment in mice. *Aging Cell*. 2021;20(2):e13296.
69. Talma N, Gerrits E, Wang B, Eggen BJL, Demaria M. Identification of distinct and age-dependent p16High microglia subtypes. *Aging Cell*. 2021;20(10):e13450.
70. Wang B, Wang L, Gasek NS, Zhou Y, Kim T, Guo C, et al. An inducible p21-Cre mouse model to monitor and manipulate p21-highly-expressing senescent cells in vivo. *Nat Aging*. 2021;1(10):962–73.
71. Hsu CH, Altschuler SJ, Wu LF. Patterns of early p21 dynamics determine proliferation-senescence cell fate after chemotherapy. *Cell*. 2019;178(2):361–373.e12.
72. Amulic B, Knackstedt SL, Abu Abed U, Deigendesch N, Harbort CJ, Caffrey BE, et al. Cell-cycle proteins control production of neutrophil extracellular traps. *Dev Cell*. 2017;43(4):449–462.e5.
73. Hall BM, Balan V, Gleiberman AS, Strom E, Krasnov P, Virtuoso LP, et al. p16(Ink4a) and senescence-associated β -galactosidase can be induced in macrophages as part of a reversible response to physiological stimuli. *Aging*. 2017;9(8):1867–84.
74. Rackov G, Hernández-Jiménez E, Shokri R, Carmona-Rodríguez L, Mañes S, Álvarez-Mon M, et al. p21 mediates macrophage reprogramming through regulation of p50–p50 NF- κ B and IFN- β . *J Clin Invest*. 2016;126(8):3089–103.
75. Haston S, Gonzalez-Gualda E, Morsli S, Ge J, Reen V, Calderwood A, et al. Clearance of senescent macrophages ameliorates tumorigenesis in KRAS-driven lung cancer. *Cancer Cell*. 2023;41(7):1242–1260.e6.
76. Prieto LI, Sturmlechner I, Graves SI, Zhang C, Goplen NP, Yi ES, et al. Senescent alveolar macrophages promote early-stage lung tumorigenesis. *Cancer Cell*. 2023;41(7):1261–1275.e6.
77. Behmoaras J, Gil J. Similarities and interplay between senescent cells and macrophages. *J Cell Biol*. 2021;220(2):e202010162.
78. Avelar RA, Duffield T, Lagger C, Krstevska N, Breuer M, De Magalhães JP. Mosaic regulation of stress pathways underlies senescent cell heterogeneity. *Bioinformatics*. 2024. <https://doi.org/10.1101/2024.10.03.616489>.
79. Ximerakis M, Lipnick SL, Innes BT, Simmons SK, Adiconis X, Dionne D, et al. Single-cell transcriptomic profiling of the aging mouse brain. *Nat Neurosci*. 2019;22(10):1696–708.
80. Cai Y, Zhou H, Zhu Y, Sun Q, Ji Y, Xue A, et al. Elimination of senescent cells by β -galactosidase-targeted prodrug attenuates inflammation and restores physical function in aged mice. *Cell Res*. 2020;30(7):574–89.
81. L'Hôte V, Mann C, Thuret JY. From the divergence of senescent cell fates to mechanisms and selectivity of senolytic drugs. *Open Biol*. 2022;12(9):220171.
82. Atkinson JR, Jerome AD, Sas AR, Munie A, Wang C, Ma A, et al. Biological aging of CNS-resident cells alters the clinical course and immunopathology of autoimmune demyelinating disease. *JCI Insight*. 2022;7(12):e158153.
83. Constantinescu CS, Farooqi N, O'Brien K, Gran B. Experimental autoimmune encephalomyelitis (EAE) as a model for multiple sclerosis (MS). *Br J Pharmacol*. 2011;164(4):1079–106.
84. Ransohoff RM. Animal models of multiple sclerosis: the good, the bad and the bottom line. *Nat Neurosci*. 2012;15(8):1074–7.
85. Melchor GS, Khan T, Reger JF, Huang JK. Remyelination pharmacotherapy investigations highlight diverse mechanisms underlying multiple sclerosis progression. *ACS Pharmacol Transl Sci*. 2019;2(6):372–86.
86. Baker D, Nutma E, O'Shea H, Cooke A, Orian JM, Amor S. Autoimmune encephalomyelitis in NOD mice is not initially a progressive multiple sclerosis model. *Ann Clin Transl Neurol*. 2019;6(8):1362–72.
87. Caravagna C, Jaouën A, Desplat-Jégo S, Fenrich KK, Bergot E, Luche H, et al. Diversity of innate immune cell subsets across spatial and temporal scales in an EAE mouse model. *Sci Rep*. 2018;8:5146.
88. Absinta M, Lassmann H, Trapp BD. Mechanisms underlying progression in multiple sclerosis. *Curr Opin Neurol*. 2020;33(3):277–85.
89. Moseley CE, Virupakshiah A, Forsthuber TG, Steinman L, Waubant E, Zamvil SS. MOG CNS Autoimmunity and MOGAD. *Neurol Neuroimmunol Neuroinflammation*. 2024;11(5): e200275.
90. Hafemeister C, Satija R. Normalization and variance stabilization of single-cell RNA-seq data using regularized negative binomial regression. *Genome Biol*. 2019;20(1):296.
91. Choudhary S, Satija R. Comparison and evaluation of statistical error models for scRNA-seq. *Genome Biol*. 2022;23(1):27.

Publisher's Note

Springer Nature remains neutral with regard to jurisdictional claims in published maps and institutional affiliations.